On the penetration of reactive oxygen and nitrogen species (RONS) across the stratum corneum

Jiangwei Duan[1,2,3,a)], Mingyu Ma[1,a)], Maksudbek Yusupov[3], Rodrigo M. Cordeiro[4], Xinpei Lu[1,2,b)], Annemie Bogaerts[3,b)]

[1]*State Key Laboratory of Advanced Electromagnetic Engineering and Technology, School of Electrical and Electronic Engineering, Huazhong University of Science and Technology, Wuhan 430074, China*

[2]*IFSA Collaborative Innovation Center, Shanghai Jiao Tong University, Shanghai 200240, P.R. China*

[3]*Research group PLASMANT, Department of Chemistry, University of Antwerp, Antwerp-Wilrijk, Belgium*

[4]*Centro de Ciências Naturais e Humanas, Universidade Federal do ABC, Avenida dos Estados 5001, 09210-580 Santo André, SP, Brazil*

[a)]Jiangwei Duan and Mingyu Ma contributed equally to this work.

[b)]Authors to whom correspondence should be addressed: luxinpei@hotmail.com and

annemie.bogaerts@uantwerpen.be

Abstract:

The penetration of reactive oxygen and nitrogen species (RONS) across the stratum corneum (SC) is a necessary and crucial process in many skin-related plasma medical applications. To gain more insights in this penetration behavior, we combined experimental measurements of the permeability of dry and moist SC layers, with computer simulations of model lipid membranes. We measured the permeation of relatively stable molecules which are typically generated by plasma, namely H_2O_2, NO_3^- and NO_2^-. Furthermore, we calculated the permeation free energy profiles of the major plasma-generated RONS and their derivatives (i.e., H_2O_2, OH, HO_2, O_2, O_3, NO, NO_2, N_2O_4, HNO_2, HNO_3, NO_2^- and NO_3^-) across native and oxidized SC lipid bilayers, in order to understand the mechanisms of RONS permeation across the SC. Our results indicate that hydrophobic RONS (i.e., NO, NO_2, O_2, O_3 and N_2O_4) translocate easier across the SC lipid bilayer than hydrophilic RONS (i.e., H_2O_2, OH, HO_2, HNO_2, and HNO_3) and ions (i.e., NO_2^- and NO_3^-) that experience much higher permeation barriers. The permeability of RONS through the SC skin lipids is enhanced when the skin is moist and the lipids are oxidized.

These findings may help to understand the underlying mechanisms of plasma interaction with bio-material and to optimize the environmental parameters in practice in plasma medical applications.

1. Introduction

Cold atmospheric plasma is gaining increasing interest for many medical applications, such as wound healing [1-3], skin disease treatment [4, 5], and cancer therapy [6-8]. It is a cocktail that consists of various physical and chemical components, including electrons, ions, neutrals, strong electric field, heat and ultraviolet (UV) light, which may influence the therapeutic effects. Among these components, the reactive oxygen and nitrogen species (ROS and RNS, or RONS), generated by the plasma are regarded as the main contributors to its therapeutic effects [9]. They include among others H_2O_2, OH, O, $^1O_2$, O_3, NO, NO_2, HOONO, and the concentration of these plasma-generated RONS can vary depending on the discharge and feed gas parameters. Note that we also include relatively stable species such as NO_2^- and NO_3^- under the designation of RONS because they are typical end-products of RONS reactions.

RONS are able to affect the cell proliferation [10], migration [11] and apoptosis [12, 13] via lipid oxidization [14], DNA damage [15, 16] or cell signaling activations [17]. These species are also able to stimulate the immune responses by regulating the release of immune-related factors [18] and affecting the immune cells [19]. However, in practice, for many skin-related applications, these reactive species must be delivered into the skin, reaching a deeper target, in order to achieve their therapeutic effects [20]. In this process, they need to penetrate through the stratum corneum (SC) first.

The SC is the outermost layer of the skin, which plays the most important role in the skin barrier function, preventing the penetration of compounds into the body via the epidermis. The structure of the SC is often described as a "brick-and-mortar" structure, in which the corneocytes represent the bricks and the lipids correspond to the mortar. The corneocytes are the dead and keratin-rich cells, which are surrounded by a mixture of intercellular lipids. These lipids are organized into a multilamellar structure that is the only continuous structure in the SC. There are two transepidermal penetration pathways for a molecule permeating through the SC layer: transcellular route and

intercellular route. The transcellular route mainly penetrating through the corneocytes directly and the intercellular route mainly penetrating through the intercellular lipids. It is believed by many researchers that the intercellular route is main penetration pathway for most of components [21]. Besides, for the molecule permeating through SC layer via transcellular pathway, it requires not only partitioning through the keratin bricks but also across the intercellular lipids. Thus, the intercellular lipids are important for both pathways playing a major role in the barrier nature of the SC, even for the molecule permeating through transcellular route.

It is reported that the major intercellular lipids of the SC are ceramides, free fatty acids and cholesterol [22-24]. In order to investigate the characters of the lipid mixture and the penetration of some components across the SC layer, the MD simulations are widely used. In MD simulations, the SC lipid mixture is simplified in a lipid bilayer composed of ceramides, free fatty acids and cholesterol molecules. With the lipid bilayer model, the characters of the SC barrier and the penetration of some molecules are investigated successfully [25-27], which indicates it is a useful tool and even can be used for drugs designing in drug delivery system [28, 29].

Considering the very strong barrier effects of the SC and the important role of RONS in plasma medical applications, it is essential to investigate the penetration process of RONS across the SC layer [30]. Thus, in this study we carried out experiments and molecular dynamics (MD) simulations to address these questions. Experimentally, we measured the long-lived species (H_2O_2, NO_3^- and NO_2^-) generated by the plasma, penetrating through and stored in dry and moist SC layers. By means of MD simulations, we investigated the permeation processes of the main plasma-generated RONS (i.e., H_2O_2, OH, HO_2, O_2, O_3, NO, NO_2, N_2O_4, HNO_2, HNO_3, NO_2^-, NO_3^-) across native and oxidized SC lipid bilayers.

2. Experiments

2.1. Preparation of the SC samples

The SC samples (Figure 1B) are isolated from porcine ear skin (Figure 1A), which has similar characteristics as human skin and is usually used for dermatopharmacokinetic studies *in vitro* [31, 32]. The subcutaneous fat of skin samples

isolated from the ear was first removed, and then the samples were immersed into 0.25 % trypsin-EDTA (Gibco, USA) at 37 °C for 48h. After the immersion, the SC layer was peeled off with tweezers. Finally, after washing with water and air-drying, the SC layers were instantly used as biological samples for the experiments.
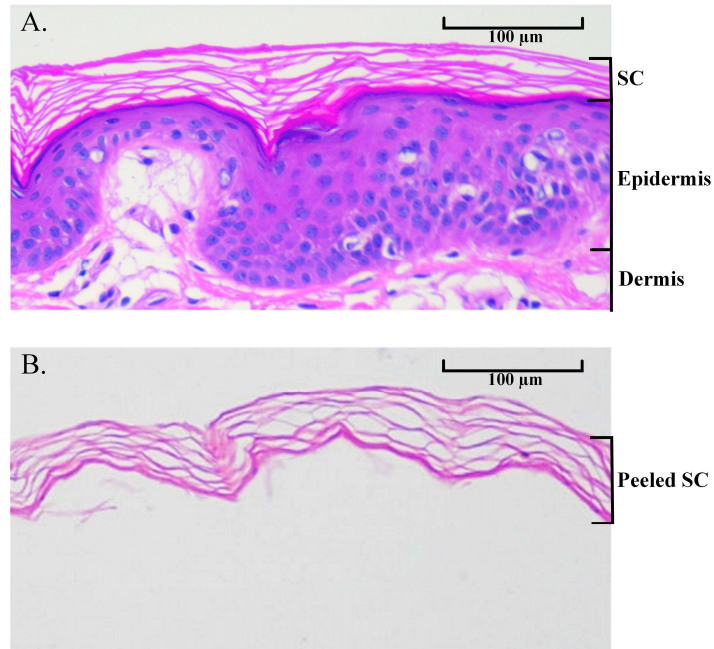

Figure 1. A. HE (Hematoxylin-Eosin) staining of normal porcine ear skin, showing the SC, epidermis, and part of dermis. B. The intact SC layer was used in this experiment, which was peeled from the normal porcine ear skin.
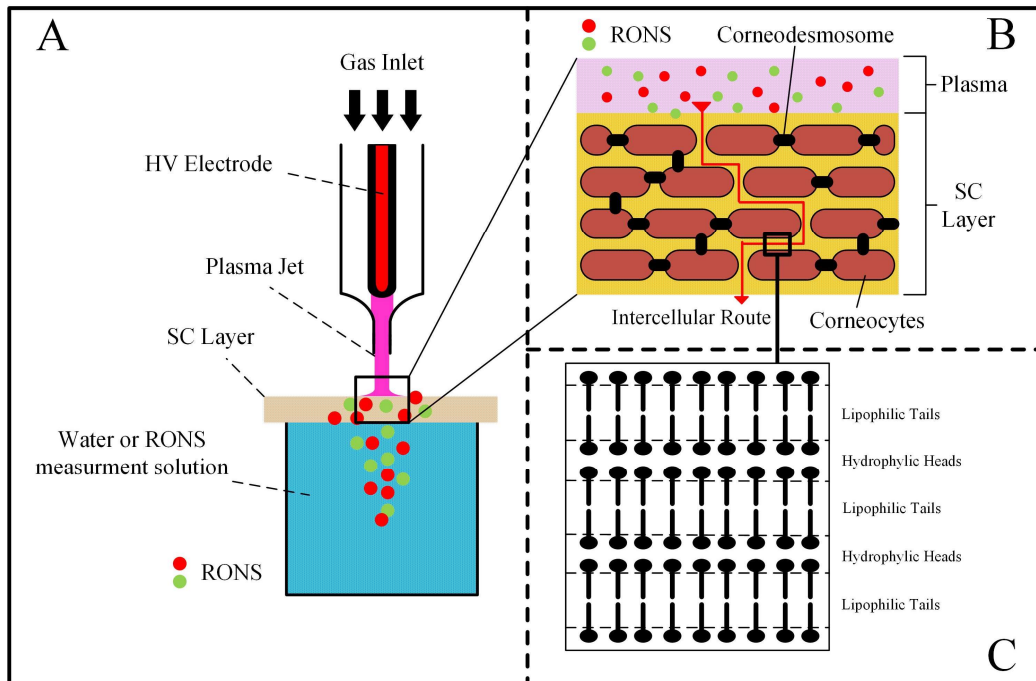
2.2. Experimental setup

Figure 2. A. Schematic diagram of the experimental setup. A fresh dry or moist SC layer was put on a receiving well and treated with a plasma jet. After plasma treatment, the concentration of H_2O_2, NO_3^- and NO_2^- penetrating through and stored in the SC layer was measured. For H_2O_2 and NO_3^- measurement, the liquid in the receiving well was pure water (pH = 7); for NO_2^- measurement, the liquid in the receiving well was Griess reagent (pH < 7) because the NO_2^- is not very stable. B. The "brick-and-mortar" structure of the SC. The corneocytes (bricks) are embedded in the matrix of special lipids (mortar) that consist of mainly ceramides, free fatty acids and cholesterol [22-24], and most of components permeate through the SC by the intercellular route (mortar). C. The highly ordered structure of the lipid matrix consisting of stacked lipid layers.

Figure 2 illustrates the experimental setup. The fresh SC layer, which was dried by using bibulous paper or kept moist by putting 100 µL of water on top of it, covers the receiving well (volume: 360 µL, area: 0.32 cm^2 per well) and was treated by a plasma jet for different times (0, 5, 10, 15, 20 min). After plasma treatment, the concentration of H_2O_2, NO_3^- and NO_2^- dissolved into the receiving well and stored in the SC layer were measured immediately. Three fresh SC layers were used for statistical

analysis for every treatment time.

The parameters of the plasma jet were adjusted carefully to avoid the destruction of the SC layer. An alternating current (AC) with a peak-to-peak voltage of 15 kV and a frequency of 1 kHz was applied to generate plasma. The gas flow was a mixture of helium flow at 2 L/min and oxygen flow at 10 mL/min. The distance between the jet nozzle and the surface of the SC layer was 1 cm.

2.3. Preparation of the SC sample extracts

The extracts of SC samples were prepared to measure the RONS stored in the SC layer after plasma treatment. The samples were ground by manual quartz grinders with 1 mL pre-cooling water, and then the suspensions were centrifuged at 10000 r/min for 5 min. The concentrations of H_2O_2, NO_3^- and NO_2^- were measured in the supernatant liquid.

2.4. RONS measurements

The concentrations of H_2O_2, NO_3^- and NO_2^- were measured after plasma treatment by the following methods [33, 34].

H_2O_2 was measured with Hydrogen Peroxide assay kit (Beyotime, China). 100 μL of test solutions mixed with 100 μL of liquid sample were put at room temperature for 30 min and measured immediately with a microplate reader at a wavelength of 570 nm. The detection limit was 1 μM.

NO_3^- was measured with Nitric Oxide (NO) assay kit (Nitrate reductase method, Nanjing Jiancheng Bioengineering Institute, China) according to the protocol. NO_3^- was transformed into NO_2^- induced by nitrate reductase, and then the NO_2^- concentration was measured by the Griess reagent with a microplate reader at a wavelength of 550 nm.

NO_2^- was measured with Nitrite Assay Kit (Nanjing Jiancheng Bioengineering Institute, China) which is a kind of Griess reagent. For the NO_2^- penetration detection, the test solution was directly put in the receiving wells. For measuring the NO_2^- in the SC samples, 100 μL of test solution mixed with 100 μL of liquid sample was placed at

room temperature for 15 min. The colorimetric results were measured at 550 nm by a microplate reader, and the detection limit was 1 μM.

2.5. Statistical analysis

All of the experiments were performed in triplicate. The results are presented as Mean ± Standard Deviation (SD).

3. Computer simulations

3.1 Preparation of the model systems

In order to have an atomic level understanding of the permeation of different RONS across the native SC layer, and investigate the effects of oxidation induced by plasma on the RONS translocation, we performed MD simulations. Among all of lipid composition in SC layer, the polyunsaturated fatty acid component is particularly susceptible to peroxidation and can undergo significant change, and 5α-CH is the predominant oxidized species which is responsible for the structural changes [35]. Thus, 5α-CH was chosen to build the oxidized SC lipid bilayer. Native and 100% oxidized skin lipid bilayer models were built based on literature [35, 36]. Specifically, the model systems in our simulations contain a certain number of lipid molecules, such as ceramide (CER), free fatty acid (FFA), cholesterol (CHO) and oxidized cholesterol (5α-CH) molecules, where the latter was used in our oxidized model system (see Figure 3A).
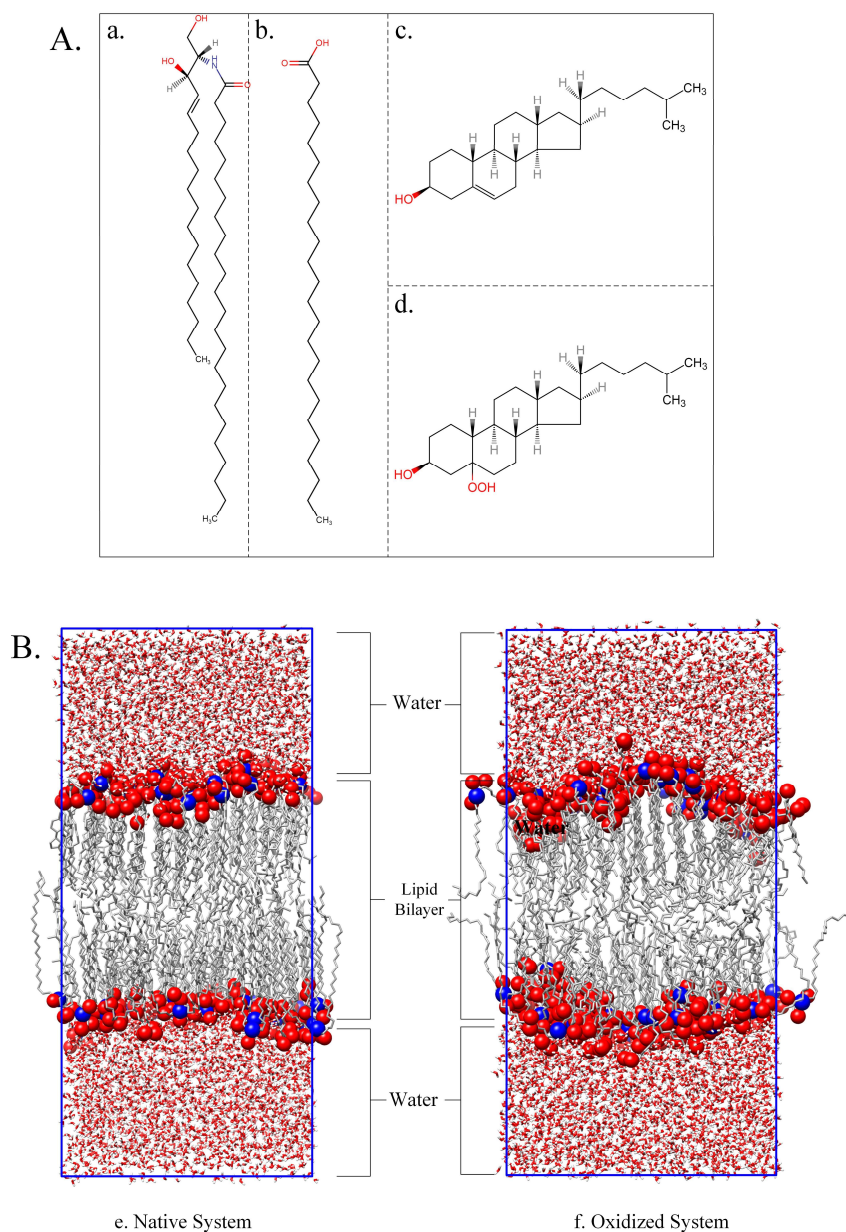
Figure 3. A. Skin lipid molecules used to build the model systems, (a) ceramide (CER), (b) free fatty acid (FFA), (c) cholesterol (CHO) and (d) oxidized cholesterol (5α-CH). B. The model systems used in our simulations, (e) the native system consisting of 52 CERs, 52 FFAs, 50 CHOs and 5120 water molecules and (f) the oxidized system containing 52 CERs, 52 FFAs, 50 5α-CHs and 5120 water molecules. As is clear, the native and oxidized model systems differ only in (un)oxidized CHO molecules. The O atoms of all lipid molecules and N atoms of CERs are marked with red and blue, respectively. For clarity, these atoms are depicted with bigger beads.

The initial structures of the model lipid bilayers were constructed by the PACKMOL package [37]. Both the native and oxidized lipid bilayers contain 52 CERs and 52 FFAs as well as either 50 CHOs (in the native system) or 50 5α-CHs (in the oxidized system), equally distributed in both layers and covered with water molecules on top and at the bottom (see Figure 3B). Thus, the CHOs of the native system are entirely (100%) oxidized into 5α-CH in the oxidized system.

All the MD simulations were performed using the GROMACS 2018.3 package [38]. The GROMOS-type force field parameters were used for the interatomic interactions. The parameters of the CER, FFA and CHO were based on Berger [39] and Holtje [40]. The parameters of the 5α-CH were taken from [41]. The RONS parameters were obtained from references [42-45]. It is noted that HNO_2 has two configurations, i.e., *trans*HONO and *cis*HONO, and both of them were studied in this research. The simple point charge (SPC) model was used for the water molecules.

It should be noted that the force field we used is a non-reactive force field, which does not allow the breaking and formation of bonds, therefore, chemical reactions of the RONS with the lipids and water could not be included during the simulations. However, these MD simulations can provide some valuable insights for the permeabilities of RONS based on their physical characters, including the charge of particles, the polarity of particles, the Van der Waals interactions and even the H-bond interactions.

The native and oxidized skin lipid bilayers were first energy-minimized with the steepest descent algorithm, and then equilibrated with the isothermal-isobaric (NPT) ensemble for 50 ps at 1 bar and 310.15 K using a time step of 0.5 fs, to release the bad contacts in the systems. After that, again the NPT ensemble was run for 150 ns at 1 bar and 310.15 K using a time step of 2 fs. The temperature was controlled by the Nose-Hoover thermostat combined with a coupling constant of 0.5 ps, and the pressure was controlled by the semi-isotropic Parrinello-Rahman barostat combined with a coupling constant of 2 ps and compressibility of 4.5×10^{-5} bar^{-1}. The cut-off distance for van der Waals interactions was set at 1.0 nm and the Particle Mesh Ewald (PME) method was

applied to calculate electrostatic interactions. Periodic boundary conditions were applied in all three directions.

3.2 Calculation of the free energy profiles

In order to investigate the transport of different RONS across the native and oxidized SC layers, the permeation free energy profiles (FEPs) of RONS (i.e., H_2O_2, OH, HO_2, O_2, O_3, NO, NO_2, N_2O_4, HNO_2, HNO_3, NO_2^-, NO_3^-) through the native and pre-oxidized skin lipid bilayers were calculated applying the umbrella sampling (US) method. Specifically, to obtain the average FEP of each electroneutral RONS (i.e., H_2O_2, OH, HO_2, O_2, O_3, NO, NO_2, N_2O_4, HNO_2, HNO_3) for each model system, five structures of lipid bilayers were used, which were derived from the last 50 ns of equilibration runs. For calculation of each individual FEP, 176 US windows were defined in the z-axis (i.e., along the bilayer normal), separated by 0.5 Å. In each US simulation, 32 individual particles (e.g., H_2O_2) were inserted into the system, distributed over 8 planes along the z-axis (i.e., 4 particles in each plane) and separated by 1.1 nm from each other in the z-axis. Thus, by performing 22 (176/8) US simulations, we obtained four FEPs, each ranging from -4.4 to 4.4 nm in the z-axis. The movement of the inserted particles was restrained along the z-axis by a harmonic bias with force constant of 2000 kJ•mol^{-1}•nm^{-2}. They were also restrained to move in the xy-plane by applying the flat-bottomed position restraint, with a radius of 0.5 nm and a force constant of 1000 kJ•mol-1•nm^{-2}. Thus, in this way we were able to reduce the computational costs. Each US simulation lasted 20 ns and the last 10 ns were used as sampling time (i.e., for collection of data). Note that this time was sufficient to obtain symmetric FEPs (i.e., symmetric to the center of the bilayer), which are indicative of proper convergence of the free energy simulations. In total, the FEP of each electroneutral RONS was obtained from 110 (5×22) US simulations and averaged over 20 (5×4) individual FEPs. The FEPs were constructed applying a periodic version of the weighted histogram analysis method (WHAM) [46], by using the *gmx wham* tool of GROMACS. In the case of HNO_2, two different sets of simulations were compared, each one starting from either the *cis* or the *trans* configuration of HNO_2 and allowing transitions to occur.

We cannot use the same procedure for the ions (NO_2^- and NO_3^-) as applied above for the electroneutral RONS, since too many ions in the system (i.e., 32) leads to a disruption of the lipid model systems. Indeed, our test simulations showed the destruction of the bilayer systems. To solve this problem, we applied the following procedure for the ions. To calculate the FEPs of the ions (NO_2^- and NO_3^-) across the SC layers, we used three structures of lipid bilayers (i.e., three for the native and three for the oxidized system), derived from the last 50 ns of equilibration runs. For each US simulation, the starting structures (i.e., US windows) were obtained by pulling the center of mass of each ion across the lipid bilayers with a force constant of 2000 kJ/mol and a slow pulling rate of 0.0001 nm/ps. Thus, in each US simulation we used a single target anion, which does not lead to a disturbance of the system. To keep the system electrically neutral, a Na^+ was added to the system by replacing the water molecule randomly in each US simulation. For one individual FEP calculation, 89 US windows were defined, separated by 1 Å along the z-axis. The FEPs were again constructed by the WHAM method [46]. Each US simulation lasted 20 ns and the last 10 ns simulation time was used for the construction of the FEP. In total, 267 (3×89) US simulations were carried out for each ion to obtain the averaged FEP.

3.3 Calculation of the area per lipid (APL) and bilayer thickness

The average area per lipid (APL) and the average thickness of both native and oxidized bilayers were calculated by the GridMAT-MD package [47]. Specifically, the APL was determined by dividing the surface area of the SC bilayer by the total number of lipids (including CHO/5α-CH) of one layer, i.e., $L_x \times L_y/77$, where L_x and L_y are the x and y dimensions of the bilayer, respectively, and 77 is the number of lipids present in one layer. The bilayer thickness was determined by averaging all distances (z-components) between the O atoms of the two opposite layers of the SC bilayer. The last 50 ns of the equilibration simulations was used for obtaining the average APL and bilayer thickness.

4. Results and discussion

4.1. H_2O_2 measurement

The concentrations of H_2O_2 permeating across and stored in the SC layer after different plasma treatment times are presented in Figure 4. The results show that, in the absence of a SC layer, the concentration of H_2O_2 in the receiving well increases with treatment time, and is up to 285.7 ± 13.3 μM after 20 min plasma treatment (see Figure 4A). However, no H_2O_2 signals can be measured after plasma treatment, when the receiving well is covered with dry SC layer. On the other hand, when the receiving well is covered by moist SC layer, few H_2O_2 can be measured in the receiving well after 15 min (1.6 ± 0.3 μM) and 20 min (2.7 ± 0.2 μM) plasma treatment (see Figure 4A). Thus, H_2O_2 generated by the plasma jet cannot permeate across the dry SC layer and slightly permeates across the moist SC layer at a long treatment time under the experimental conditions used in this study. The number of H_2O_2 stored in the SC layer after plasma treatment is shown in Figure 4B. As is clear, the amount of H_2O_2 remaining in the SC layer increases with treatment time, and more H_2O_2 are stored in the SC layer when it is moist. For example, after 20 min plasma treatment, the density of H_2O_2 stored in the moist SC layer is $84.3\pm10.8 \times10^{14}/cm^2$, which is about two times higher than the density of H_2O_2 stored in the dry SC layer ($45.7\pm1.7 \times10^{14}/cm^2$), see Figure 4B.
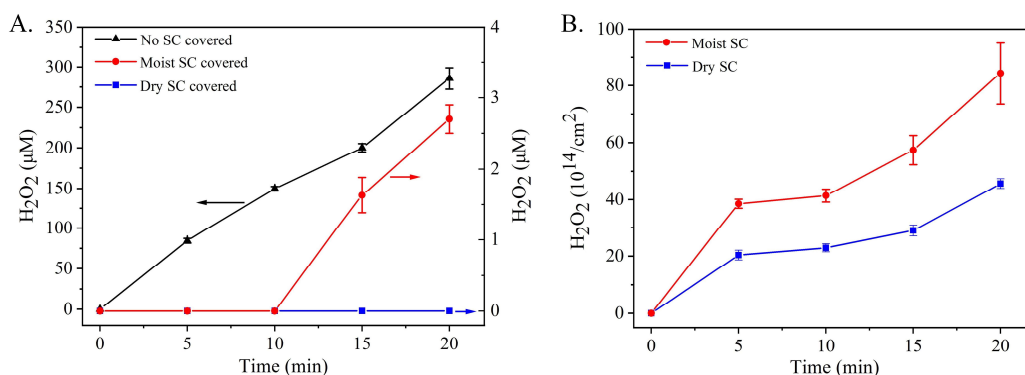

Figure 4. (A) The concentration of H_2O_2 in the water-containing receiving well after plasma treatment, when not covered by SC, and when covered by either moist or dry SC. (B) The number of H_2O_2 molecules per square centimeter left in the SC layer after plasma treatment, for either moist or dry SC.

4.2. NO_3^- measurement

The concentration of NO_3^- in the receiving well (i.e., after penetrating the SC layer) and stored in the SC layer also increases with increasing plasma treatment time (Figure 5). As is clear from Figure 5A, after 20 min plasma treatment, the concentration of NO_3^- permeating across the dry and moist SC layer is 3.6 ± 0.3 μM and 4.2 ± 0.2 μM, respectively, which is about one-ninth or one-eighth of the NO_3^- concentration measured in the absence of a SC layer (31.6 ± 2.7 μM). Furthermore, the density of NO_3^- stored in the moist SC layer is slightly higher than in the dry SC layer (see Figure 5B). For example, after 20 min plasma treatment, the density of NO_3^- stored in the moist SC layer is $55.6\pm4.6 \times10^{14}/cm^2$, while it is $42.6\pm2.7 \times10^{14}/cm^2$ in the dry SC layer.
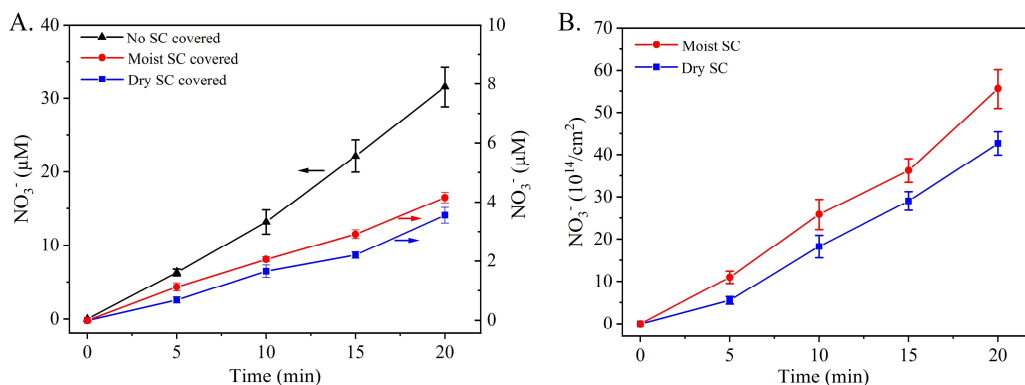

Figure 5. (A) The concentration of NO_3^- in the water-containing receiving well after plasma treatment, when not covered by SC, and when covered by either moist or dry SC. (B) The number of NO_3^- molecules per square centimeter left in the SC layer after plasma treatment, for either moist or dry SC.

4.3. NO_2^- measurement

The concentration of NO_2^- in the receiving well (i.e., after penetrating the SC layer) and stored in the SC layer after different plasma treatment times is shown in Figure 6. In all conditions (i.e., with and without SC layer covering the well) the concentration of NO_2^- in the receiving well is about several micromolar, and it increases with treatment time. When the receiving well is covered with the SC layer, the concentration of NO_2^- permeating across this layer is 1.3 ± 0.1 μM (dry SC layer) or 2.0 ± 0.1 μM (moist

SC layer) after 20 min plasma treatment, which is around one third or a half of the NO_2^- concentration measured without SC layer (i.e., 4.3 ± 0.3 μM, see Figure 6A). Furthermore, the density of NO_2^- stored in the SC layer increases with plasma treatment time, and more NO_2^- is stored in the moist SC layer compared to the dry SC layer (see Figure 6B). For example, after 20 min plasma treatment, the density of NO_2^- stored in the moist SC layer (i.e., $23.4\pm1.4 \times10^{14}/cm^2$) is about three times higher than that in the dry SC layer (i.e., $8.7\pm1.6 \times10^{14}/cm^2$).
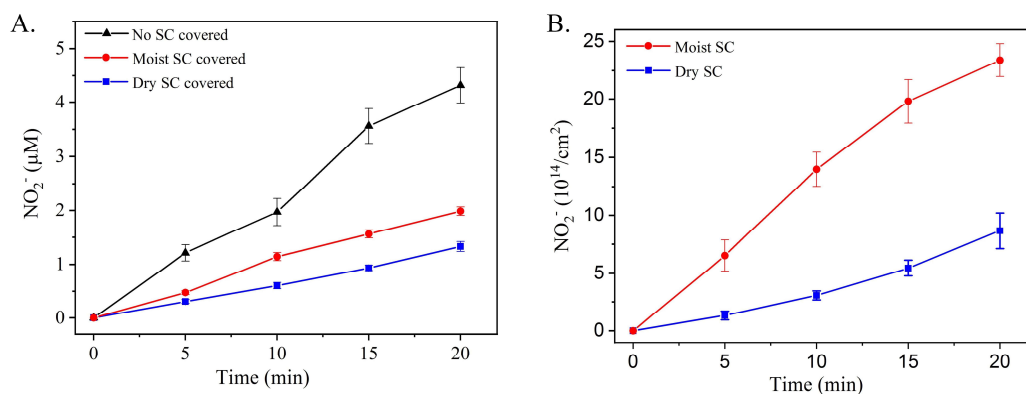

Figure 6. (A) The concentration of NO_2^- in the water-containing receiving well after plasma treatment, when not covered by SC, and when covered by either moist or dry SC. (B) The number of NO_2^- molecules per square centimeter left in the SC layer after plasma treatment, for either moist or dry SC.

Thus, from Figures 4-6 we can conclude that the permeabilities of the plasma-generated long-lived species (H_2O_2, NO_3^- and NO_2^-) are different. H_2O_2 cannot penetrate across the dry SC, and slightly penetrates through the moist SC at a long plasma treatment time. NO_3^- and NO_2^- can penetrate the SC in both dry and moist conditions. All the species can be stored in the SC layer, which is enhanced in the case of moist SC layer.

4.4. Effect of moisture of the SC layer on the RONS penetration and storage

The results of the previous section indicate that more RONS, especially H_2O_2, can penetrate through and be stored in the moist SC layer than in the dry SC layer at a long

treatment time. This may be caused by the different amounts of H_2O_2 produced in these layers and by the different permeation efficiency of RONS in these two layers.

In a cold plasma jet, H_2O_2 is mainly formed by the recombination of OH radicals that are created upon dissociation of water molecules (see reactions 1 and 2 below) [48, 49]. Hence, the water molecules are the crucial source for generation of H_2O_2. It is reported that the H_2O_2 concentration in a cold plasma jet increases linearly with increasing humidity of the feed gas [50]. In our experiments, more H_2O_2 is produced on the top surface of the moist SC layer than of the dry SC layer, causing more H_2O_2 penetration and storage in the moist SC layer (see Figure 4).

$$H_2O \ + \ P \ \rightarrow \ \bullet OH \ + \ \bullet H + P \tag{1}$$

$$\bullet OH \ + \ \bullet OH \ + \ M \rightarrow H_2O_2 \ + \ M \tag{2}$$
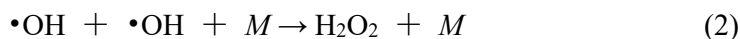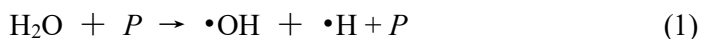
where P is an energetic particle (e.g. electron or excited helium atom) and M is an arbitrary collision partner (e.g. helium).

On the other hand, the moisture of the SC may also influence the penetration of other RONS. Previous research indicates that aqueous plasma-activated species penetrate mouse skin easier than gaseous plasma-activated species, which was attributed to the different penetration pathways [51]. In drug penetration field, keeping water in the skin can enhance the penetration of most of drugs, which may result from the stratum corneum hydration increasing and swelling corneocytes [52]. When the SC layer is moist, the gaseous plasma-activated species convert into aqueous species at first, and then penetrate through the SC layer, causing more RONS permeation than the direct gaseous plasma-activated species permeation (i.e., when the SC layer is dry). Thus, our results indicate that the bio-effects induced by cold plasma may be enhanced when the surface of the skin is moist.

4.5. Penetration of different RONS

As mentioned in the Introduction, various ROS and RNS are generated by the plasma jet, and they are regarded as the main contributors to the plasma medicine

applications. According to the literature [30, 53], the most relevant ROS in plasma are atomic oxygen (O), singlet delta oxygen ($^1O_2$), superoxide (O_2^-), ozone (O_3), hydroxyl radicals (OH) and hydrogen peroxide (H_2O_2), whereas the most relevant RNS are nitric oxide (NO), nitrogen dioxide (NO_2), and peroxynitrite ($ONOO^-$). Nitrite (HNO_2/NO_2^-) and nitrate (HNO_3/NO_3^-) can also be generated as stable end-products of RONS reactions. Some of these RONS (such as O and OH) exhibit strong oxidative properties, causing modification of lipids, proteins and DNA, resulting in alterations in cells. Other RONS (like NO) act as the regulator of cellular function, affecting the cell proliferations or immune responses [54, 55]. When the skin is exposed to plasma, the RONS in the plasma should penetrate through the SC layer, reaching the deeper target, to achieve its therapeutic goal.

Previous researches indicate short-lived RONS hardly penetrate through the SC layer due to their strong reactive character, resulting in a half-life time of several nanoseconds [30]. On the other hand, long-lived RONS have a longer half-life time, but they can also be consumed and trapped by the SC layer.

In order to quantize the effects of SC layer on the long-lived RONS penetration, we calculated the blocking ratio of moist SC layer and dry SC layer with followed formula:

$$k_b = \left(1 - \frac{c_1}{c_2}\right) \times 100\%$$

Where k_b is the blocking ratio of the SC layer for a specific reactive specie; c_1 is the concentration of a specific reactive specie in the receiving wells after plasma treatment when the wells were covered with SC layer; c_2 is the concentration of a specific reactive specie in the receiving wells when no SC layer covered. It should be noted that the blocking ratio k_b in general indicates the effects of SC layer on the RONS penetrations compared with no SC layer covered situations. The contributions of RONS productions, the RONS consumption by SC layer, and the different permeabilities of RONS across the SC layer are all reflected in the blocking ratio.

The blocking ratios of moist SC layer and dry layer on long-lived RONS after 20 min plasma treatment are presented in table 1, which shows that approximately 99.1%

of H_2O_2 is blocked by the moist SC layer and almost all of them are blocked from permeation by the dry SC layer. For the penetrations of NO_3^- ions, it is clear from Table 1 that 86.7% of NO_3^- is blocked by the moist SC layer and 88.6% is blocked by the dry SC layer. Similarly, for the NO_2^- penetration, 53.5% of NO_2^- is blocked by the moist SC layer, whereas 69.8% is blocked by the dry SC layer.

Table 1. Blocking effect of the SC on RONS penetration, for 20 min plasma treatment.

Long-lived species	No SC covered c_2 (µM)	Moist SC covered		Dry SC covered	
		Concentration c_1 (µM)	Blocking ratio k_b (%)	Concentration c_1 (µM)	Blocking ratio k_b (%)
H_2O_2	285.7±13.3	2.7±0.2	99.1	< 1	~100
NO_3^-	31.6±2.7	4.2±0.2	86.7	3.6±0.3	88.6
NO_2^-	4.3±0.3	2.0±0.1	53.5	1.3±0.1	69.8

Thus, our experimental results indicate that H_2O_2 has the hardest penetration ability through the SC layer after plasma treatment, while NO_2^- and NO_3^- penetrate more easily through the SC layer. This phenomenon can be caused by two factors: First, H_2O_2 is consumed by the antioxidants in the SC, while these antioxidants hardly react with NO_2^- and NO_3^-. Indeed, it was reported that the antioxidant network present in the SC protects the skin from oxidative stress via antioxidants and the concentration of carotenoids in the SC decreases after plasma treatment [56]. The antioxidants in the SC include carotenoids [57], vitamin E, vitamin C, glutathione, uric acid and catalase [58, 59]. Thus, these antioxidants can react with H_2O_2, thereby resulting in a lower permeability of H_2O_2. As is clear from Figures 4A, 5A and 6A above, H_2O_2 is the only species among the investigated substances that exhibits a kind of "delay time" in its permeation behavior. In other words, in the case of moist SC layer the H_2O_2 concentration in the receiving well remains zero at the beginning and starts to increase only after about 10 min (Figure 4A), whereas other species (NO_2^- and NO_3^-) permeate from the very

beginning (see Figures 5A and 6A). Thus, we can assume that there is a high probability of H_2O_2 consumption by antioxidants at the beginning of the experiment. Only after the effect of antioxidants, H_2O_2 manages to pass through the SC layer, therefore having in general the hardest penetration ability. Second, the SC has a different barrier effect for H_2O_2 molecule than for NO_2^- and/or NO_3^-. This might also be the reason for the higher storage of H_2O_2 than the other species after plasma treatment. This effect will be discussed in detail in section 4.6.

As we mentioned, after plasma treatment, a lot of RONS are stored in the SC layer, indicating that the SC layer acts as a RONS receiving pool when treated by the plasma, which is also linked with the strong barrier effects of the SC.

4.6. FEPs of RONS across the SC lipid bilayers

In order to study the transport of RONS across the SC layer, the FEPs of some typical RONS (H_2O_2, OH, HO_2, O_2, O_3, NO, NO_2, N_2O_4, HNO_2, HNO_3, NO_2^- and NO_3^-) through the native and oxidized SC lipid bilayers were calculated by means of MD simulations.
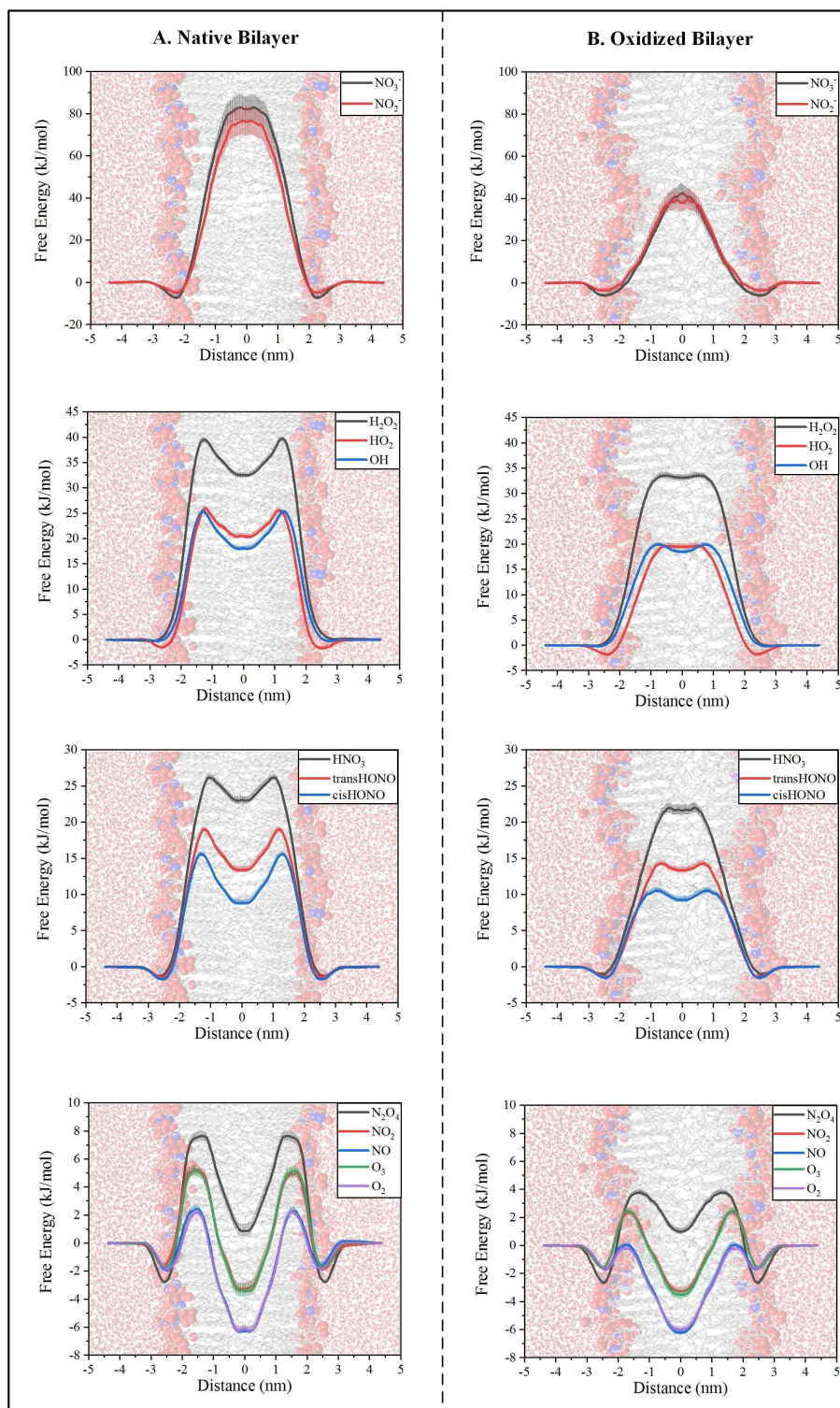
Figure 7. FEPs of typical RONS (NO_3^-, NO_2^-, H_2O_2, HO_2, OH, HNO_3, HNO_2 (i.e., *trans*HONO and *cis*HONO), N_2O_4, NO_2, NO, O_3, O_2) across the native (A) and oxidized (B) SC lipid bilayers. For clarity, the lipid bilayers are illustrated in the background.

The results are presented in Figure 7, and the transfer free energies (ΔG) of the various RONS across the native and oxidized SC lipid bilayers are summarized in Table 2 (ordered from the highest to the lowest values).

Table 2. Transfer free energies (ΔG) of RONS across the SC lipid bilayers.

Species	ΔG (kJ/mol)	
	Native	Pre-oxidized
NO_3^-	83.05±5.82	42.53±4.30
NO_2^-	76.71±6.42	39.49±4.35
H_2O_2	39.59±0.47	33.59±0.52
HNO_3	26.18±0.36	22.00±0.63
OH	25.93±0.34	20.00±0.34
HO_2	25.93±0.49	19.82±0.52
*trans*HONO	18.99±0.28	14.30±0.34
*cis*HONO	15.58±0.26	10.54±0.32
N_2O_4	7.64±0.33	3.87±0.18
NO_2	5.27±0.31	2.34±0.20
O_3	5.16±0.31	2.46±0.21
NO	2.35±0.18	0.02±0.14
O_2 ($^1O_2$)	2.19±0.17	-0.15±0.14

The results show that the ions (NO_3^- and NO_2^-) have a Λ-shaped free energy profile with the highest permeation barriers across the SC lipid bilayers (Figure 7). In nature, ions hardly permeate across the cell lipid membrane by passive diffusion, due to their higher hydration free energies and the strong absorption by the hydrophilic lipid heads [60], and they always need typical channels (anion transport proteins) to be transported [61]. Similarly, in our SC lipid bilayer, NO_3^- and NO_2^- have the highest transfer free energies (83.05 and 76.71 kJ/mol, respectively), see Table 2. The results also show that

NO_3^- and NO_2^- have similar FEPs (see Figure 7), which may result from the special permeation mechanism of ions, called ion-induced-defect-driven permeabilities [62]. Under this permeation mechanism, the interface between the water and lipid bilayer is reshaped due to the force of ions, and ions have the similar free energy profiles despite they have different chemical composition, size, and hydration free energy.

The transfer free energies of all other electroneutral species, from water to the center of the lipid bilayer show a similar profile (see Figure 7A), i.e., they first decrease near the water-lipid interface and then increase, reaching their maximum values in the lipid region, followed by a decrease in the center of the bilayer. All hydrophilic species (i.e., H_2O_2, OH, HO_2, HNO_2 and HNO_3) [63] have minimum energies close to the water-lipid interface, which mainly results from the H-bonding and dispersion interactions between these RONS and the head groups of the bilayer [42, 44]. The hydrophobic RONS (i.e., O_2, O_3, NO, NO_2 and N_2O_4) [63], on the other hand, have their minimum energies (i.e., lower than in water) in the center of the bilayer, except for N_2O_4 that has a slightly higher energy (~1 kJ/mol) than in water (see Figure 7A).

Our simulation results show that the hydrophobic species (O_2, O_3, NO, NO_2 and N_2O_4) have lower barriers than the hydrophilic species (H_2O_2, OH, HO_2, HNO_2, HNO_3) to transport to the bilayer center (see Table 2). Experiments also showed that hydrophilic solutions hardly permeate through the skin layer [64].

Our experimental results showed that the SC layer has the highest barrier for H_2O_2 penetration compared to NO_3^- and NO_2^- (see blocking ratios in Table 1). On the other hand, our MD simulations show that the transfer free energies of NO_3^- and NO_2^- (i.e., 83.05 kJ/mol and 76.71 kJ/mol) are much bigger than that of H_2O_2 across the native SC lipid bilayers (i.e., 39.59 kJ/mol). This indicates that the NO_3^- and NO_2^- concentrations measured in the receiving wells (in our experiments) are probably not due to NO_3^- and NO_2^- directly penetrating through the SC layer. There are two transform routes that may cause these results: (1) NO_3^- and NO_2^- probably originate from HNO_3 and HNO_2 penetrating through the SC layer. Acids (i.e., HNO_3 and HNO_2) are produced during the plasma treatment and they have a lower barrier for permeation across the SC lipid bilayer compared to their ionic forms (i.e., NO_3^- and NO_2^-), see Figure 7A. Thus, the

NO_3^- and NO_2^- measured in the receiving wells may be derived from the penetrations of their acid forms (i.e., HNO_2 and HNO_3). (2) The gaseous RNS (NO and NO_2), which have very low barriers to translocate across the SC lipid bilayer (see Figure 7A), penetrate the SC layer first, and then convert into NO_2^- and NO_3^-. NO_2^- and NO_3^- are the final products of reactions (3) and (4). Further research is needed to verify the contributions of these two pathways.

$$NO_2 + NO_2 + H_2O \rightarrow NO_2^- + NO_3^- + 2H^+ \tag{3}$$

$$NO + NO_2 + H_2O \rightarrow 2NO_2^- + 2H^+ \tag{4}$$
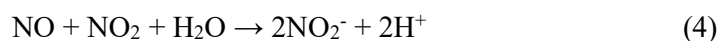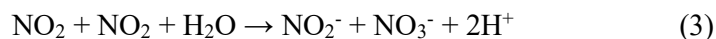
Thus, our simulation results indicate that the permeability of typical ROS, like H_2O_2, OH, HO_2, across the skin lipids is much lower (due to much higher barriers, or transfer free energies) than for typical RNS (NO, NO_2, N_2O_4) and O_2, O_3, indicating that RNS and O_2, O_3 may play an important role in plasma medicine applications.

4.7. Penetration of RONS across oxidized SC lipid bilayers

We also investigated the oxidation effect of lipids on the RONS penetration across the SC lipid bilayer by the MD simulations (Figure 7B). In our model, we assumed that all of the CHOs (Figure 3c) are oxidized to 5α-CHs (Figure 3d). Our results show that the oxidation of CHOs leads to a decrease of the permeation barriers of all RONS. Especially the permeation barriers of the ions (NO_3^- and NO_2^-) are reduced to a larger extent than the other electroneutral species. Thus, in general, RONS penetrate across the SC lipid bilayers easier when the lipids are oxidized. This is due to the instability of the lipid bilayers caused by oxidization. From Figure 3B, we can clearly see that the oxidized lipid bilayer loses its highly-ordered arrangements. The calculated area per lipid (APL) and thickness of the bilayer are presented in Table 3. It is clear that the APL increases and the bilayer thickness decreases as the CHO lipids are oxidized; the interspaces between lipids in the water-lipid interface increase, which results in easier penetrations of RONS across the bilayer.

Table 3. Average APL and thickness of the native and oxidized bilayer.

	APL (nm^2)	Thickness (nm)
Native bilayer	0.340 ± 0.003	4.832 ± 0.259
Oxidized bilayer	0.353 ± 0.005	4.623 ± 0.425

5. Conclusions

Our experimental results indicate that the penetration of RONS across the SC layer increases when the SC layer is moist compared with dry SC layer, and our MD simulation results indicate that the permeability of RONS across the SC lipid bilayer is enhanced when the lipids are oxidized. These results may help to increase the effects of cold plasma in medical applications. Moreover, the simulation results indicate that the RNS (NO, NO_2, N_2O_4) as well as O_2, O_3 penetrate the SC layer easier than the hydrophilic ROS (H_2O_2, OH, HO_2), which may contribute to a better understanding of the therapeutic effects of cold atmospheric plasma.

References:
[1] A. Schmidt, S. Bekeschus, K. Wende, B. Vollmar, and T. von Woedtke, *Exp. Dermatol.* **2017**, *26*, 156.
[2] J. Gao, L. Wang, C. Xia, X. Yang, Z. Cao, L. Zheng, R. Ko, C. Shen, C. Yang, and

C. Cheng, *Int. Wound J.* **2019**, *16*, 1103.

[3] A. Schmidt and S. Bekeschus, *Antioxidants* **2018**, *7*, 146.

[4] T. Bernhardt, M.L. Semmler, M. Schäfer, S. Bekeschus, S. Emmert, and L. Boeckmann, *Oxid. Med. Cell. Longev.* **2019**, *2019*, 10.

[5] L. Gan, J. Duan, S. Zhang, X. Liu, D. Poorun, X. Liu, X. Lu, X. Duan, D. Liu, and H. Chen, *Free Radic. Res.* **2019**, *53*, 1.

[6] H.-R. Metelmann, C. Seebauer, V. Miller, A. Fridman, G. Bauer, D.B. Graves, J.-M. Pouvesle, R. Rutkowski, M. Schuster, S. Bekeschus, K. Wende, K. Masur, S. Hasse, T. Gerling, M. Hori, H. Tanaka, E.H. Choi, K.-D. Weltmann, P.H. Metelmann, D.D. Von Hoff, and T. von Woedtke, *Clin. Plasma Med.* **2018**, *9*, 6.

[7] M. Ma, J. Duan, X. Lu, and G. He, *Phys. Plasmas* **2019**, *26*, 23523.

[8] M. Keidar, D. Yan, I.I. Beilis, B. Trink, and J.H. Sherman, *Trends Biotechnol.* **2018**, *36*, 586.

[9] X. Lu, G. V. Naidis, M. Laroussi, S. Reuter, D.B. Graves, and K. Ostrikov, *Phys. Rep.* **2016**, *630*, 1.

[10] S. Hasse, T. Duong Tran, O. Hahn, S. Kindler, H.-R. Metelmann, T. von Woedtke, and K. Masur, *Clin. Exp. Dermatol.* **2016**, *41*, 202.

[11] A. Schmidt, S. Bekeschus, T. von Woedtke, and S. Hasse, *Clin. Plasma Med.* **2015**, *3*, 24.

[12] S.J. Kim and T.H. Chung, *Sci. Rep.* **2016**, *6*, 20332.

[13] J. Duan, X. Lu, and G. He, *J. Appl. Phys.* **2017**, *121*, 13302.

[14] M. Yusupov, K. Wende, S. Kupsch, E.C. Neyts, S. Reuter, and A. Bogaerts, *Sci. Rep.* **2017**, *7*, 5761.

[15] L. Guo, Y. Zhao, D. Liu, Z. Liu, C. Chen, R. Xu, M. Tian, X. Wang, H. Chen, and M.G. Kong, *Free Radic. Res.* **2018**, *52*, 783.

[16] A.M. Hirst, M.S. Simms, V.M. Mann, N.J. Maitland, D. O'Connell, and F.M. Frame, *Br. J. Cancer* **2015**, *112*, 1536.

[17] S. Bekeschus, A. Schmidt, L. Bethge, K. Masur, T. von Woedtke, S. Hasse, and K. Wende, *Oxid. Med. Cell. Longev.* **2016**, *2016*, 11.

[18] N.K. Kaushik, N. Kaushik, B. Min, K.H. Choi, Y.J. Hong, V. Miller, A. Fridman, and E.H. Choi, *J. Phys. D. Appl. Phys.* **2016**, *49*, 84001.

[19] A. Lin, B. Truong, G. Fridman, A.A. Fridman, and V. Miller, *Plasma Med.* **2017**, *7*, 85.

[20] E.J. Szili, J.-S. Oh, H. Fukuhara, R. Bhatia, N. Gaur, C.K. Nguyen, S.-H. Hong, S. Ito, K. Ogawa, and C. Kawada, *Plasma Sources Sci. Technol.* **2017**, *27*, 014001.

[21] Haque, Tasnuva, and Md Mesbah Uddin Talukder. *Adv Pharm Bull.* **2018**, *8*, 169.

[22] C.R. Harding, *Dermatol. Ther.* **2004**, *17*, 6.

[23] J. van Smeden and J.A. Bouwstra, *Curr. Probl. Dermatol.* **2016**, pp. 8–26.

[24] G.K. Menon, G.W. Cleary, and M.E. Lane, *Int. J. Pharm.* **2012**, *435*, 3.

[25] Das, Chinmay, Massimo G. Noro, and Peter D. Olmsted. *Biophys. J.* **2009**, *97*, 1941.

[26] Notman, Rebecca, and Jamshed Anwar. *Adv. Drug Deliv. Rev.* **2013**, *65*, 237.

[27] M. Lundborg, C.L. Wennberg, A. Narangifard, E. Lindahl, and L. Norlén, *J. Control. Release* **2018**, *283*, 269.

[28] Al-Qattan, Mohammed N., Pran Kishore Deb, and Rakesh K. Tekade. *Drug Discov Today* **2018**, *23*, 235.

[29] J. Torin Huzil, S. Sivaloganathan, M. Kohandel, and M. Foldvari, *Wiley Interdiscip. Rev. Nanomedicine Nanobiotechnology* **2011**, *3*, 449.

[30] X. Lu, M. Keidar, M. Laroussi, E. Choi, E.J. Szili, and K. Ostrikov, *Mater. Sci. Eng. R Reports* **2019**, *138*, 36.

[31] U. Jacobi, M. Kaiser, R. Toll, S. Mangelsdorf, H. Audring, N. Otberg, W. Sterry, and J. Lademann, *Ski. Res. Technol.* **2007**, *13*, 19.

[32] C. Herkenne, A. Naik, Y.N. Kalia, J. Hadgraft, and R.H. Guy, *Pharm. Res.* **2006**, *23*, 1850.

[33] Y. Yang, Z. Li, L. Nie, and X. Lu, *J. Appl. Phys.* **2019**, *125*, 223302.

[34] J. Duan, L. Gan, L. Nie, F. Sun, X. Lu, and G. He, *Phys. Plasmas* **2019**, *26*, 43504.

[35] S. Kumar, D.K. Yadav, E.H. Choi, and M.H. Kim, *Sci. Rep.* **2018**, *8*, 1.

[36] D.K. Yadav, S. Kumar, E.-H. Choi, P. Sharma, S. Misra, and M.-H. Kim, *Front. Pharmacol.* **2018**, *9*, 644.

[37] L. Martínez, R. Andrade, E.G. Birgin, and J.M. Martínez, *J. Comput. Chem.* **2009**, *30*, 2157.

[38] M.J. Abraham, T. Murtola, R. Schulz, S. Páll, J.C. Smith, B. Hess, and E. Lindahl, *SoftwareX* **2015**, *1–2*, 19 .

[39] O. Berger, O. Edholm, and F. Jähnig, *Biophys. J.* **1997**, *72*, 2002.

[40] M. Höltje, T. Förster, B. Brandt, T. Engels, W. von Rybinski, and H.-D. Höltje, *Biochim. Biophys. Acta - Biomembr.* **2001**, *1511*, 156.

[41] A.J.P. Neto and R.M. Cordeiro, *Biochim. Biophys. Acta - Biomembr.* **2016**, *1858*, 2191.

[42] R.M. Cordeiro, *Biochim. Biophys. Acta - Biomembr.* **2014**, *1838*, 438.

[43] R. M. Cordeiro, *J. Phys. Chem. B* **2018**, *122*, 8211.

[44] J. Razzokov, M. Yusupov, R.M. Cordeiro, and A. Bogaerts, *J. Phys. D. Appl. Phys.* **2018**, *51*, 365203.

[45] R.M. Cordeiro, M. Yusupov, J. Razzokov, and A. Bogaerts, *J. Phys. Chem. B* **2020**, *124*, 1082-10.

[46] J.S. Hub, B.L. de Groot, and D. van der Spoel, *J. Chem. Theory Comput.* **2010**, *6*, 3713.

[47] W.J. Allen, J.A. Lemkul, and D.R. Bevan, *J. Comput. Chem.* **2009**, *30*, 1952.

[48] J. Winter, H. Tresp, M.U. Hammer, S. Iseni, S. Kupsch, A. Schmidt-Bleker, K. Wende, M. Duennbier, K. Masur, K.-D. Weltmannan, and S. Reuter, *J. Phys. D. Appl. Phys.* **2014**, *47*, 285401.

[49] P. Bruggeman and D.C. Schram, *Plasma Sources Sci. Technol.* **2010**, *19*, 45025.

[50] J. Winter, K. Wende, K. Masur, S. Iseni, M. Dünnbier, M.U. Hammer, H. Tresp, K.-D. Weltmann, and S. Reuter, *J. Phys. D. Appl. Phys.* **2013**, *46*, 295401.

[51] X. Liu, L. Gan, M. Ma, S. Zhang, J. Liu, H. Chen, D. Liu, and X. Lu, *J. Phys. D. Appl. Phys.* **2018**, *51*, 75401.

[52] Zhai, Hongbo, and Howard I. Maibach. *Skin Pharmacol. Appl. Skin Physiol.* **2001**, *14*, 1.

[53] Y. Gorbanev, A. Privat-Maldonado, and A. Bogaerts, *Anal. Chem.* **2018**, *90*, 13151.

[54] U. Förstermann and W.C. Sessa, *Eur. Heart J.* **2011**, *33*, 829.

[55] D. Tousoulis, A.-M. Kampoli, C. Tentolouris Nikolaos Papageorgiou, and C. Stefanadis, *Curr. Vasc. Pharmacol.* **2012**, *10*, 4.

[56] J.W. Fluhr, S. Sassning, O. Lademann, M.E. Darvin, S. Schanzer, A. Kramer, H. Richter, W. Sterry, and J. Lademann, *Exp. Dermatol.* **2012**, *21*, 130.

[57] Lademann J., Schanzer S., Meinke M., Sterry W. and Darvin M.E. *Skin Pharmacol. Physiol.* **2011**, *24*, 238.

[58] J.J. Thiele, C. Schroeter , S.N. Hsieh, M. Podda, and L. Packer, *Oxid. Antioxidants Cutan. Biol.* **2001**, pp. 26–42.

[59] J.J. Thiele, *Skin Pharmacol. Physiol.* **2001**, *14*, 87.

[60] A.P. Davis, D.N. Sheppard, and B.D. Smith, *Chem. Soc. Rev.* **2007**, *36*, 348.

[61] A.J. Miller, X. Fan, M. Orsel, S.J. Smith, and D.M. Wells, *J. Exp. Bot.* **2007**, *58*, 2297.

[62] I. Vorobyov, T.E. Olson, J.H. Kim, R.E. Koeppe, O.S. Andersen, and T.W. Allen, *Biophys. J.* **2014**, *106*, 586.

[63] R. Vácha, P. Slavíček, M. Mucha, B.J. Finlayson-Pitts, and P. Jungwirth, *J. Phys. Chem. A* **2004**, *108*, 11573

[64] L. Chen, L. Han, and G. Lian, *Adv. Drug Deliv. Rev.* **2013**, *65*, 295.

Table 1. Blocking effect of the SC on RONS penetration, for 20 min plasma treatment.

Long-lived species	No SC covered c_2 (μM)	Moist SC covered		Dry SC covered	
		Concentration c_1 (μM)	Blocking ratio k_b (%)	Concentration c_1 (μM)	Blocking ratio k_b (%)
H_2O_2	285.7±13.3	2.7±0.2	99.1	< 1	~100
NO_3^-	31.6±2.7	4.2±0.2	86.7	3.6±0.3	88.6
NO_2^-	4.3±0.3	2.0±0.1	53.5	1.3±0.1	69.8

Table 2. Transfer free energies (ΔG) of RONS across the SC lipid bilayers.

Species	ΔG (kJ/mol)	
	Native	Pre-oxidized

NO$_3^-$	83.05±5.82	42.53±4.30
NO$_2^-$	76.71±6.42	39.49±4.35
H$_2$O$_2$	39.59±0.47	33.59±0.52
HNO$_3$	26.18±0.36	22.00±0.63
OH	25.93±0.34	20.00±0.34
HO$_2$	25.93±0.49	19.82±0.52
*trans*HONO	18.99±0.28	14.30±0.34
*cis*HONO	15.58±0.26	10.54±0.32
N$_2$O$_4$	7.64±0.33	3.87±0.18
NO$_2$	5.27±0.31	2.34±0.20
O$_3$	5.16±0.31	2.46±0.21
NO	2.35±0.18	0.02±0.14
O$_2$ (^{1}O$_2$)	2.19±0.17	-0.15±0.14

Table 3. Average APL and thickness of the native and oxidized bilayer.

	APL (nm^2)	Thickness (nm)
Native bilayer	0.340 ± 0.003	4.832 ± 0.259
Oxidized bilayer	0.353 ± 0.005	4.623 ± 0.425

Table of Contents: The penetration of reactive oxygen and nitrogen species (RONS) across the stratum corneum (SC) is a crucial process in skin-related plasma medical

applications. To gain more insight in this penetration process, experiments and molecular dynamics (MD) simulations were carried out. Our results show the different pemeabilities of different kinds of RONS, which may help to understand the underlying mechanisms of plasma interaction with bio-material.

Graphic for the 'Summary' and the 'Table of Contents':